

# Variations of stress parameters in the Southern California plate boundary around the South Central Transverse Ranges

Niloufar Abolfathian<sup>1</sup>, Patricia Martínez-Garzón<sup>2</sup>, and Yehuda Ben-Zion<sup>1</sup>

<sup>1</sup>University of Southern California

<sup>2</sup>Helmholtz Centre Potsdam GFZ German Research for Geosciences

November 22, 2022

## Abstract

We examine stress parameters in Southern California with a focus on the region near the South Central Transverse Ranges (SCTR), using a refined stress inversion methodology to 1981-2017 declustered and aftershocks focal mechanisms independently. Comparison between the associated stress parameters provides information on the local dominant loading. The estimated stress parameters are examined in relation to the regional stress regime and local loadings. Over the regional scale, the Strends towards the NNE and the stress ratios vary from transtensional stress regime near the Eastern California Shear Zone (ECSZ), to shear stress near the SCTR, and towards transpression near the Western Transverse Ranges. Detailed analysis of stress parameters near the SCTR indicates deviations from the regional shear stress. The San Bernardino Mountain area shows S direction towards NNW and transpressional stress components likely associated with the relative motion of the San Andreas Fault and ECSZ. The Cajon Pass and San Gorgonio Pass show transpressional stress regime near the bottom of the seismogenic zones likely associated with the elevated topography. In Crafton Hills, rotation of the principal stress plunges and S direction and transtensional stress regime below  $\sim 10$  km, along with lower estimated apparent friction coefficient suggest a weak fault possibly associated with deep creep. The results reveal effects of local loadings resolved by the performed multi-scale analysis. The study does not show significant temporal variations of stress variations near the SCTR from the average stress parameters in the analyzed 37 years.

1 **Variations of stress parameters in the Southern California plate boundary around**  
2 **the South Central Transverse Ranges**

3  
4  
5 Niloufar Abolfathian<sup>1</sup>, Patricia Martínez-Garzón<sup>2</sup>, Yehuda Ben-Zion<sup>1</sup>

6  
7 <sup>1</sup>University of Southern California, Los Angeles, USA

8 <sup>2</sup>GFZ German Research Centre for Geosciences, Potsdam, Germany

9  
10  
11  
12 **Three key points of the research:**

13 (1) Local stress deviations from the regional stress field provide information on  
14 dominant local loadings.

15 (2) Comparing stress field inversions using declustered seismicity and aftershocks  
16 help to identify the main loading in an area.

17 (3) Higher topography produces compressional stress components at the bottom  
18 of the seismogenic zone.

32  
33  
34  
35  
36  
37  
38  
39  
40  
41  
42  
43  
44  
45  
46  
47  
48  
49  
50  
51  
52  
53  
54  
55  
56  
57  
58  
59  
60  
61  
62

**Abstract**

We examine stress parameters in Southern California with a focus on the region near the South Central Transverse Ranges (SCTR), using a refined stress inversion methodology to 1981-2017 declustered and aftershocks focal mechanisms independently. Comparison between the associated stress parameters provides information on the local dominant loading. The estimated stress parameters are examined in relation to the regional stress regime and local loadings. Over the regional scale, the  $S_{Hmax}$  trends towards the NNE and the stress ratios vary from transtensional stress regime near the Eastern California Shear Zone (ECSZ), to shear stress near the SCTR, and towards transpression near the Western Transverse Ranges. Detailed analysis of stress parameters near the SCTR indicates deviations from the regional shear stress. The San Bernardino Mountain area shows  $S_{Hmax}$  direction towards NNW and transpressional stress components likely associated with the relative motion of the San Andreas Fault and ECSZ. The Cajon Pass and San Gorgonio Pass show transpressional stress regime near the bottom of the seismogenic zones likely associated with the elevated topography. In Crafton Hills, rotation of the principal stress plunges and  $S_{Hmax}$  direction and transtensional stress regime below  $\sim 10$  km, along with lower estimated apparent friction coefficient suggest a weak fault possibly associated with deep creep. The results reveal effects of local loadings resolved by the performed multi-scale analysis. The study does not show significant temporal variations of stress variations near the SCTR from the average stress parameters in the analyzed 37 years.

**Index Terms and Keywords**

Stress, stress inversion, South Central Transverse Ranges, aftershocks, fault loading.

63

## 1. Introduction

64           The boundary between the North American and Pacific plates in Southern  
65 California consists of multiple active fault zones with different total offsets, slip rates and  
66 seismic activities (Figure 1). Most of the plate boundary motion and seismic hazard are  
67 associated with the San Andreas Fault (SAF) and San Jacinto Fault Zone (SJFZ). The  
68 plate boundary in the South Central Transverse Ranges (SCTR) with high topography of  
69 ~3 km associated with the San Gabriel and San Bernardino Mountains has a complex set  
70 of thrust and strike-slip faults (e.g., Matti et al., 1993; Spotila et al., 2001; Yule and Sieh,  
71 2003), especially between Cajon Pass (CP) and San Gorgonio Pass (SGP). The Crafton  
72 Hills (CH) area between the SAF and SJFZ has significant seismicity that is relatively  
73 deep (Figure 1). Improved characterization of the stress field within and around the  
74 SCTR area can provide useful information on tectonic deformation and earthquake  
75 processes in the region. This is done in the present paper with stress inversion analyses of  
76 earthquake focal mechanisms on regional and local scales.

77           Previous studies examined the stress field around the SCTR and other regions in  
78 Southern California. Hardebeck and Hauksson (2001) performed stress inversion of focal  
79 mechanisms and showed that a homogeneous background stress field is not able to  
80 explain the complex faulting system and stress variations in the region. They also studied  
81 the temporal changes of stress variations in 5-year time periods between 1980 and 1999.  
82 Their results show significant changes in the orientations of the maximum horizontal  
83 compressional stress in the vicinity of major earthquakes, and no significant changes  
84 detectable within the noise level of the data related to the tectonic loading. Yang and  
85 Hauksson (2013) studied stress parameters on regional (100-500 km resolution) and local  
86 scales (less than 100km) and discussed the importance of local scale stress variations that  
87 can affect rupture zones of major M7 type earthquakes.

88           In the present study we use earthquake fault plane solutions from 1981 to 2017 to  
89 examine the 3D background stress field in a regional scale (Figure 1) extending from the  
90 Eastern California Shear Zone (ECSZ) to the LA basin (section 4.1), along with more  
91 detailed spatiotemporal variations of the stress field employing fault plane solutions of  
92 earthquakes from 1981 to 2017 (section 4.2). Employing a refined stress inversion  
93 methodology developed by Martínez-Garzón et al. (2016a), over larger data set compared

94 with previous studies, we obtain more stable stress parameters in a finer resolution of ~5  
95 km (resolution varies with the seismicity distribution) that provide information on the  
96 local stress field and associated loadings in more detail than earlier works.

97 Various studies indicate that focal planes of aftershocks are in general consistent  
98 with the orientation of the major geological structures (McCloskey et al., 2003;  
99 Hardebeck, 2014). The total crustal stress field ( $\tau_T$ ) can be written as the sum

100

$$101 \quad \tau_T = \tau_R + \tau_L + \Delta\tau_{ST}. \quad (1)$$

102

103 where  $\tau_R$  is the regional far field loading,  $\tau_L$  represents additional loading due to local  
104 features such as topography, and  $\Delta\tau_{ST}$  is stress transfer from earthquakes in the  
105 considered crustal volume.

106 Inversions of focal mechanisms of declustered seismicity (mainshocks) provide  
107 information on the background stress field associated with the loading components  
108 ( $\tau_R + \tau_L$ ), while inversions of the aftershock mechanisms reflect the background stress  
109 field together with the internal stress transfers of the mainshocks and these events  
110 ( $\tau_R + \tau_L + \Delta\tau_{ST}$ ). Comparing the stress fields produced by these two types of inversion  
111 can provide information on the dominant loading mechanisms of the mainshocks that  
112 drive the aftershocks. In section 4.3 we compare the estimated stress parameters from the  
113 mainshocks and the aftershocks in the focused study area around the SCTR.

114

## 115 **2. Data and the study area**

116 For the purpose of this study, the earthquake hypocenters are selected from the  
117 Southern California relocated catalog of Hauksson et al. (2012, extended to later years)  
118 (Figure 1) with horizontal and vertical location errors of 0.75 km and 1.25 km,  
119 respectively. The fault plane solutions are selected from the Yang et al. (2012, extended  
120 to later years) focal mechanism catalog for the total time period of 1981-2017. The  
121 selected focal mechanisms have qualities from A to D, in accordance with 5° to 55°  
122 degrees of uncertainty, where with the mentioned uncertainty range, inversions with ~40  
123 events per grid cell, resolves a stable stress field (Martínez-Garzón et al., 2016a).

124 The selected focal mechanism catalog is declustered using the nearest-neighbor

125 proximity approach developed by Zaliapin and Ben-Zion (2013, 2020), separating the  
126 mainshock events from the aftershocks and the foreshocks. The declustered seismicity  
127 makes it possible to focus on the background tectonic stress, and separately on the stress  
128 field associated with internal stress transfers resulting the aftershocks (Martínez-Garzón  
129 et al., 2016a). The declustered events are also referred to as background seismicity.

130 The background hypocenters show notable variations in the selected focused area  
131 near the SCTR. The area between the main two faults of SAF and SJFZ includes 52% of  
132 all the selected background seismicity and has the deepest seismogenic thickness (defined  
133 as the depth above which 90% of the events are located) of 17.8 km (Figure 1). The  
134 background seismicity from east of the SAF comprises 34% of the selected events and  
135 displays a seismogenic thickness of 11.9 km, while the western section of the SJFZ  
136 includes 14% of the background seismicity and has a seismogenic thickness of 14.9 km.  
137 Based on the mentioned background seismicity hypocentral variations and the geological  
138 structures such as mountain ranges and the main faults we divided the area into six sub-  
139 regions (Figure 2). The sub-regions are as follows: (1) San Gabriel Mountains (SGM), (2)  
140 San Bernardino Mountains (SBM), two areas in the (3) northern and (4) eastern sections  
141 of the SBMs including parts of the ECSZ and fault system near Landers, (5) between the  
142 two main fault strands of SAF and SJFZ, and (6) Western region of the SJFZ. We  
143 separately analyze the background stress field of the mentioned sub-regions in the entire  
144 seismogenic thickness.

145 The stress parameters are estimated independently for the mainshocks' and  
146 aftershocks' mechanisms. Aftershocks comprise the majority of events in the SCTR  
147 (65%), while mainshocks (background events) are only 21% of the earthquakes in the  
148 selected focused study area. Should be noted that the seismogenic thickness of the  
149 mainshocks is ~16.9 km, whereas the aftershocks show a shallower seismogenic  
150 thickness of ~13.5 km in the focused study area. The ~3.4 km average hypocentral  
151 difference of the mainshocks and aftershocks is correlated with the difference in their  
152 associated main loadings. Table 1 summarizes statistical information on the distribution  
153 of the mainshocks and the aftershocks.

154

155

### 156 3. Methodology

#### 157 3.1 Stress tensor inversion of focal mechanisms

158 In this study, we apply the refined stress inversion method developed by  
159 Martínez-Garzón et al. (2016a) on double-couple earthquake focal mechanisms Catalog  
160 in Southern California. The inversion method employs the refined MSATSI software  
161 (Martínez-Garzón et al., 2014; 2016a), which is an updated version from SATSI  
162 algorithm (Michael, 1984; Hardebeck and Michael, 2006). The assumptions of the stress  
163 inversion include: (1) The stress field is homogeneous within a considered rock volume,  
164 (2) Earthquakes occur on pre-existing faults with varying orientations, and (3) Slip on  
165 each fault occurs parallel to the direction of its tangential traction (Wallace, 1951; Bott,  
166 1959).

167 The implied method includes discretizing the events based on an optimum  
168 required number of focal mechanisms per grid cell to constrain a stable stress orientation  
169 of an area (McKenzie, 1969), which in this study ~40 events is the optimum number of  
170 events per grid cell (Martínez-Garzón et al., 2016a). The study volume is discretized  
171 using the  $k$ -means technique (Hartigan and Wong, 1979; Martínez-Garzón et al., 2016a)  
172 into Voronoi grid cells containing the mentioned optimum number of events. The cell  
173 sizes vary in relation to seismicity density and provide estimates for the spatial resolution  
174 of the inversion (e.g. Figure 4).

175 The linear damped stress inversion estimates the orientations of the three principal  
176 stresses  $\sigma_1$ ,  $\sigma_2$  and  $\sigma_3$  (from most to least compressive) and the stress ratio parameter,  $R$ ,  
177 defined as

$$178 \quad R = \frac{\sigma_1 - \sigma_2}{\sigma_1 - \sigma_3} \quad (2)$$

179 The stress ratio ( $R$  value) ranges between 0 and 1, with smaller and larger stress  
180 ratios in a strike-slip environment corresponding to stress regimes closer to transtensional  
181 (i.e., mixed strike-slip and normal faulting) and transpressional (i.e., mixed strike-slip and  
182 reverse faulting) fields, respectively.

183 The orientation of maximum horizontal compressional stress,  $S_{Hmax}$ , is computed  
184 from the orientation of the principal stress axes following Lund and Townend (2007) and  
185 the estimated trends and plunges of the principal stresses are classified into Andersonian

186 stress regimes: normal, strike-slip and reverse, and oblique faulting types (Zoback, 1992).  
187 Uncertainty estimations of the inversion outputs are obtained by bootstrap resampling of  
188 the original set of focal mechanisms (Michael, 1987) and provide 95% confidence  
189 intervals.

190 The method applies an iterative procedure to select the nodal plane that is  
191 optimally oriented for failure in the estimated stress field. During each iteration, the stress  
192 field orientation is calculated and the fault plane with the largest instability coefficient  $I$  is  
193 selected for the next iteration (Vavryčuk, 2011; 2014; Martínez-Garzón et al., 2016b).  
194 The parameter  $I$  is defined as

$$195 \quad I = \frac{\tau - \mu(\sigma - 1)}{\mu + \sqrt{1 + \mu^2}}, \quad (3)$$

196 where  $\mu$  is the apparent coefficient of friction.  $\tau$  and  $\sigma$  are scaled shear and normal  
197 stresses, respectively. The parameter  $I$  takes values between 0 and 1, representing the  
198 least and most optimally oriented faults to failure within a given deviatoric stress field.  
199 When estimating the fault instability, a grid search is applied over values of coefficients  
200 of frictions, ranging between 0.2 and 0.8. For each grid cell, the estimated  $\mu$  produces the  
201 highest overall instability coefficient (Vavryčuk, 2014). Since  $\mu$  is selected based on  
202 iterative computations in the inversion procedure, we refer it as an apparent coefficient of  
203 friction.

204

## 205 **4. Results**

### 206 **4.1 Regional stress variations in Southern California**

207 Initially, we analyze the background stress distribution in a volume extending  
208 over the plate-boundary region in Southern California, from the ECSZ to the LA basin,  
209 using ~6,800 focal mechanisms from the declustered catalog between 1981-2017. To  
210 examine the 3D spatial changes of stress parameters, the selected focal mechanisms in the  
211 study area are divided into 5 km depth bins. The bin width is chosen considering the  
212 overall depth uncertainty of ~1.25 km of the resolved hypocentral locations and the  
213 optimum number of seismicity, ~40 per grid cell, in a strike-slip regime to converge to a  
214 stable stress tensor (Martínez-Garzón et al., 2016a). Focal mechanisms in each grid cell  
215 are inverted and the  $S_{Hmax}$  direction, the stress field orientations, and the stress ratio  $R$  are

216 estimated following the methodology discussed in section 3.

217 The spatial distribution of  $S_{Hmax}$  of the selected declustered seismicity over the  
218 regional scale can be divided into regions near the ECSZ, San Bernardino Mountains  
219 (SBM), the area between the SAF and SJFZ, and near the WTR (Figure 3). In the ECSZ,  
220 the  $S_{Hmax}$  is oriented toward NNE, with average azimuths of  $\sim 10^\circ$ ,  $\sim 15^\circ$  and  $\sim 12^\circ$  in the  
221 depth sections 0-5 km, 5-10 km, and 10-15 km, respectively. In the SBM, the  $S_{Hmax}$   
222 orientation rotates towards the north and slightly NNW, with average  $S_{Hmax}$  trend of  
223  $N7^\circ W$ . Between the SAF and SJFZ,  $S_{Hmax}$  generally points toward the north and NNE. In  
224 this area, near Crafton Hills, a large clockwise rotation in the  $S_{Hmax}$  direction is observed.  
225 Near the WTR and the LA basin, the  $S_{Hmax}$  directions rotate back towards NNE similar to  
226 the orientation in the ECSZ, with the difference that the WTR includes lower spatial  
227 resolution and higher uncertainty in the inferred  $S_{Hmax}$  orientation.

228 The stress regimes are estimated based on the relative position of the  $\sigma_1$ ,  $\sigma_2$ , and  
229  $\sigma_3$  axes. The regional background stress regime is in general strike-slip with deviations  
230 near the WTR deeper than 10 km showing reverse faulting and in the ECSZ, at the 5-10  
231 km depth section, showing oblique faulting with a mixture of strike-slip and normal  
232 faulting (Figure 3).

233 The variations of the estimated stress ratio  $R$  represent the deviation from the  
234 regional strike-slip faulting towards transtensional and transpressional stress regimes. In  
235 general, clear variations from transtension near the ECSZ to transpression near the WTR  
236 are observed at all depth ranges (Figure 4). Deviations from the regional strike-slip stress  
237 field near the SCTR include patches of higher transpressional components near CP and  
238 SGP (Figure 4c) and higher transtensional stress regimes observed near the CH (Figure 4,  
239 b to d). The CP, SGP, and CH areas are considered to display local stress components  
240 related to the local geological structures, which are discussed in more detail in the  
241 following section, 4.2.

242

#### 243 **4.2 Stress variations near the South Central Transverse Ranges**

244 We focus on the area near the SCTR using  $\sim 3,300$  focal mechanisms from the  
245 declustered catalog in the selected time period (brown box in Figure 1). We analyze the  
246 3D variations of the stress parameters dividing the selected focal mechanisms into 5 km

247 depth bins and the 2D spatial variation of the stress parameters dividing the background  
248 focal mechanisms based on geological features near the SCTR.

249 The  $S_{Hmax}$  orientations near the SCTR are generally towards the north and NNE  
250 direction (Figure 5), with significant variation in the CH area at 15-20 km depth, where  
251 the  $S_{Hmax}$  direction rotates  $\sim 23^\circ$  clockwise from the surface to the bottom of the  
252 seismogenic thickness (Abolfathian et al., 2019).

253 The orientations of the estimated principal stresses (shown as stereonets in Figure  
254 5) indicate the main background stress regime of strike-slip faulting, which based on the  
255 Andersonian theory of faulting has vertical intermediate principal stress and parallel least  
256 and most compressional stress orientations with the Earth surface as the reference. The  
257 Andersonian theory for strike-slip faulting holds overall from the surface to 15 km depth  
258 in the focused study area. However, below 15 km depth, the most compressive and  
259 intermediate principal stresses' plunge angles rotates about  $\sim 30^\circ$  in the CH area, and all  
260 principal stresses' plunge angles in the southern part of SGP area and close to the Hot  
261 Springs (HS) area rotate about  $\sim 15^\circ$  to  $\sim 30^\circ$  (Figure 5). In addition, in this depth section,  
262 the hypocenters of the selected focal mechanisms are mainly located between the two  
263 main faults of SAF and SJFZ.

264 Significant variations in the stress ratios are observed in the focused study area  
265 near the SCTR. In the shallowest depth bin, 0-5 km, the stress ratios follow the regional  
266 overall strike-slip faulting, varying from slightly transtensional in the most eastern  
267 section towards transpression in the most western part (Figure 4a). The same variations  
268 are observed in 5-10 km depth with amplified components of transtension and  
269 transpression in the eastern and western sections, respectively (Figure 4b). At 10-15 km  
270 depth, the higher transpressional component appears near the highest peaks of the San  
271 Bernardino Mountains near SGP, and San Gabriel Mountains close to CP (Figure 4c). At  
272 the same depth range, transtensional components emerge in the CH area. Below  $\sim 5$  km,  
273 the stress ratio near the CP area changes sharply from transpression in its northwest to  
274 transtension in its southeast, even though the inversions utilized damping to smooth stress  
275 variations between the neighbor cells. The CP area is located where the SJFZ branches  
276 from the SAF and the strong change in topography exists at the edge of the San Gabriel  
277 Mountains.

278           The region between the SJFZ and SAF near the SCTR is highly seismically active  
279 (more than 50% of the background events in the SCTR region are between the two fault  
280 strands), and the hypocenters of the declustered seismicity are on average ~5 km deeper  
281 than the ones located outside of this region. In an effort to clarify stress variations related  
282 to fault-system interactions and topographic variations, we divide selected declustered  
283 mechanisms into six sub-regions (see section 2) and invert independently for stress  
284 parameters in each sub-regions within its entire seismogenic thickness (Figure 2). The  
285 results indicate the main faulting near the SCTR is strike-slip, with deviations including  
286 amplified reverse faulting close to the CP area and oblique/normal faulting in the ECSZ  
287 area (Figure S1). The stress ratio variations from the 6 sub-regions show the  
288 compressional components near CP and the sharp stress ratio changes between the NW  
289 and SE of the junction of the SAF and SJFZ (Figure 6), where the compressional  
290 component is likely associated with the higher topography. The transtensional stress  
291 components close to the junction could be explained in terms of the extension associated  
292 with the right-lateral strike-slip motion on the SJFZ and the nearby SAF. This region also  
293 includes sub-volumes dominated by normal faulting near CH. The areas near SGP and  
294 SBM show clear transpressional components.

295           The spatio-temporal variations of background stress field are also examined and  
296 found to be in general in agreement with the discussed spatial background stress field  
297 variations (Figure S2). For this purpose, we divide the entire selected declustered focal  
298 mechanisms into 5 time periods of ~8 years, namely 1981-1985, 1986-1993, 1994-2001,  
299 2002-2009, 2010-2017, and estimate the stress parameters independently. The estimated  
300 stress parameters do not show any significant changes within these time periods.

301

### 302 **4.3 Stress variations in the SCTR — aftershocks and depth dependency**

303           In the last part, we compare the background stress variations with results obtained  
304 from the inversion of aftershocks mechanisms. The focused study area near the SCTR has  
305 ~3,300 focal mechanisms from the declustered catalog, while ~9,600 aftershock  
306 mechanisms are available in the selected area within the same time period. We divide the  
307 aftershock mechanisms in 5 km depth bins as applied on the background seismicity and  
308 invert for their stress parameters (Figure 7).

309           The transtensional component of background stress near the CH area is amplified  
310 between ~5 to 15 km depth in the stress field inverted from the aftershocks. The  
311 transpressional stress components near the SGP are also amplified in the results obtained  
312 from the aftershock mechanisms, with the difference that the areas with transpressional  
313 stress fields are located shallower compared with the ones obtained from the mainshocks.  
314 The aftershocks show the overall thinner seismogenic thickness and amplified shallower  
315 transtensional and transpressional stress components in the CH and SGP areas,  
316 respectively. In contrast, no evidence of the transpressional stress components near the  
317 CP area is observed in the aftershock results. Considering that in the CP area comprises  
318 sparse aftershock distribution, we might not have enough resolution to resolve properly  
319 the stress field from the aftershocks. The comparison of the estimated stress field from  
320 the background declustered seismicity and aftershocks help to understand the main  
321 loading in the selected area that reflect local loadings, as discussed below.

322

## 323 **5. Discussion**

324           We examine spatio-temporal variations of the stress field in the plate-boundary  
325 region around the SCTR based on inversions of earthquake focal mechanisms, and  
326 attempt to interpret the results in relation to different loadings, fault properties,  
327 topography, and crustal depth. The primary analyzed data is a declustered catalog of the  
328 focal mechanisms of Southern California earthquakes from 1981 to 2017, and is used to  
329 derive the background stress fields in different scales of space and time. We also invert  
330 separately focal mechanisms of aftershocks that are generally triggered by stress transfers  
331 from the mainshocks. Comparisons between inversion results based on the declustered  
332 seismicity and aftershocks allow us to infer dominant local loading mechanisms that exist  
333 in different crustal volumes in addition to the large-scale tectonic loading.

334           On a regional scale, the background stress fields inverted from the declustered  
335 catalog (Figures 3 and 4) are generally consistent with previous studies, showing  
336 transtensional stress regime in the ECSZ moving towards strike-slip regime near the  
337 SCTR and further transpressional stress regime in the WTR and LA basin (Hardebeck  
338 and Hauksson, 2001; Yang and Hauksson, 2013). The  $S_{Hmax}$  trends show NNE direction  
339 near the ECSZ and the WTR (Figure 3) in agreement with the regional  $S_{Hmax}$  directions in

340 Southern California (Yang and Hauksson, 2013). Various sub-volumes with clear  
341 transpressional and transtensional stress components near the SBM, CH, SGP, and CP in  
342 the SCTR do not follow the expected regional strike-slip loading and indicate additional  
343 loadings associated with local structures.

344 The stress inversion results based on the declustered catalog in the SBM show an  
345 average  $S_{Hmax}$  trend of  $N7^{\circ}W$  (Figure S1). Yang and Hauksson (2013) estimated  $S_{Hmax}$   
346 variations towards the NNW in this area and presented a schematic model of the ECSZ  
347 and SAF movements near the CP, with a wedge-shaped area of SBM having counter  
348 clock-wise loading. This scenario can induce compressional stress components near SBM  
349 that are observed ( $R \sim 0.6$ ) in the inversion results of this study (Figure 6). However, the  
350 stress field estimated from the aftershocks does not show the NNW rotation of the  $S_{Hmax}$   
351 direction and the transpressional stress components, indicating that the proposed loading  
352 in the SBM accounts only for a small fraction of the total background loading in this area.

353 Previous observations indicated tensional stress near the CH area (Hardebeck and  
354 Hauksson, 2001; Yang and Hauksson, 2013; Abolfathian et al., 2019). Several studies  
355 connected the deeper seismicity and increase of normal faulting in the northern SJFZ  
356 with deep creeping below the seismogenic fault (Wdowinski, 2009; Cooke and Beyer,  
357 2018). Our inversion results based on the declustered mechanisms are consistent with  
358 these inferences. The results of the background stress field provide the following lines of  
359 evidence that the SJFZ is weak near the bottom of the seismogenic zone in the CH area:  
360 (1) The inversion results indicate that the  $S_{Hmax}$  of the background stress field rotates  
361 clock-wise below 10 km depth, with maximum rotation at 15 km where the  $S_{Hmax}$  trend is  
362 almost perpendicular to the main surface fault trace. (2) The estimated apparent  
363 coefficient of friction indicates a weak zone with an average  $\mu$  of  $\sim 0.4$  below 10 km  
364 depth compared to an average value of  $\sim 0.55$  in the focused study area (brown box in  
365 Figure 1) (Abolfathian et al., 2019). (3) The maximum and intermediate principal stress  
366 plunges rotate more than  $45^{\circ}$  below  $\sim 12$  km depth (Abolfathian et al., 2019).

367 The stress inversions of aftershocks' mechanisms indicate transtensional  $0 < R < 0.2$   
368 stress components in the CH area (Figure 7). The aftershock results are consistent with  
369 the local background stress field estimated for the CH area rather than the regional strike-  
370 slip stress field. This suggests that the dominant loading in the CH area is associated with

371 a local structure that may be associated, as suggested in previous studies, with creep  
372 below the seismogenic fault. Evidence for a wide damage zone below 10 km in this area  
373 (Ben-Zion and Zaliapin, 2019) suggests that the deep creep may be associated with a  
374 wide shear zone rather than aseismic slip on a fault interface.

375 In the SCTR region, the SAF is associated with significant bending of the main  
376 fault by about  $\sim 20^\circ$ - $30^\circ$  and elevated terrain. The fault bending and topography are  
377 associated with perturbations in the intermediate (vertical) stress on the non-optimally  
378 oriented fault (dipping fault) at seismogenic depth (Fialko et al., 2005). The CP and SGP  
379 areas located near elevated topography in the SCTR are associated with transpression  
380 stress fields. In the SGP area, the strike-slip faulting regime is dominant from the surface  
381 to 10 km depth, while transpressional stress components are significant below 10 km.  
382 The same stress pattern exists in the CP area, with significant transpressional stress  
383 components below  $\sim 5$  km (Figure 4). The observed transpressional stress fields imply  
384 that the parts of the SAF passing through the SGP and CP may be dipping within the  
385 seismogenic depth. This is consistent with seismological observations of Fuis et al.  
386 (2012) and others.

387 The stress field estimated from the aftershock mechanisms in the SGP indicates  
388 higher compressional,  $0.8 < R < 1$ , stress components (Figure 7) and is in agreement with  
389 the loading from the topography rather than the regional strike-slip stress field,  
390 suggesting that the dominant stress field near SGP is associated with the topography (e.g.,  
391 Fialko et al., 2005). In contrast, no evidence of compressional stress components is  
392 observed in the stress field inverted from the aftershock mechanisms near CP; this may  
393 be due to the fewer available aftershock mechanisms in this area.

394 Large contrasts in the stress fields and seismicity depth are observed across the  
395 junction between the SAF and SJFZ near Cajon Pass. To the northwest of the junction in  
396 the San Gabriel Mountains the dominant stress field is transpressional ( $R \sim 0.9$ ), while to  
397 the southeast, the dominant stress field is transtensional ( $R \sim 0.2$ ) and the average  $S_{Hmax}$   
398 direction rotates more than  $15^\circ$ . The seismogenic depth varies by  $\sim 7$  km from northwest  
399 to southeast of the SAF and SJFZ junction. These variations occur over a distance less  
400 than 20 km, implying strong effects of fault properties on the stress field and the  
401 importance of high-resolution analysis of the stress field of the type done in this study.

402 Results of stress ratios inverted from the background seismicity in 5 separate time  
403 intervals of ~8 years between 1981 and 2017 are overall consistent with the discussed  
404 stress ratio variations for the combined 1981 and 2017 data, showing compressional  
405 stress components near high topography and tensional stress components near CH. The  
406 time interval 1986-1993 produces the largest transpressional stress components near the  
407 SGP area, where two transpressional events with magnitudes  $M_w$  5.6 and 5.0 occurred in  
408 1986 and 1988 (Figure S2).

409 Earthquake ruptures produce rock damage in their source volume (e.g.,  
410 Lyakhovsky et al., 1997; Lockner et al., 1992; Aben et al., 2019). The evolution of rock  
411 damage can modify the properties and dynamics of fault zones on a geological time scale  
412 (e.g., Ben-Zion and Sammis, 2003). Estimated rock damage production by ongoing  
413 background seismicity in Southern California shows several prominent damage zones  
414 (Ben-Zion and Zaliapin, 2019). The SJFZ and the SCTR, especially near major fault  
415 junctions (CP and SGP), are among the regions with the highest relative damage  
416 production, and the seismicity and rock damage become more pronounced and  
417 continuous with depth. The depth ranges with high concentration of seismicity and rock  
418 damage near CH, SGP, and CP areas are consistent with the depth range of the highest  
419 transpressional and transtensional stress components.

420 The Moho has significant depth variations below the SCTR (Zhu and Kanamori,  
421 2000; Ozakin and Ben-Zion 2015) and several studies discussed the association of Moho  
422 depth changes with enhanced generation of rock damage and reduced ability of faults to  
423 localize in the upper brittle crust (Lyakhovsky and Ben-Zion, 2009; Zaliapin and Ben-  
424 Zion, 2019). Earthquakes in such areas are expected to be distributed in space and exhibit  
425 a high diversity of mechanisms as observed near the SCTR. All three faulting types  
426 (strike-slip, reverse and normal) estimated from focal mechanisms of the declustered  
427 events exist in the entire SCTR, with increased number of normal and reverse faulting  
428 around CH and CP areas, respectively (Figure S3). The dip-slip events near the SCTR  
429 comprise a smaller fraction of the background seismicity than the strike-slip events and  
430 have mostly  $M_w < 3.5$ . The relatively small magnitudes of the dip-slip events suggest that  
431 they are mainly associated with off-fault damage zones rather than the main strike-slip  
432 plate-boundary faults. Another manifestation of complexity in the SCTR is that strike

433 angles of the declustered focal mechanisms are distributed in a range of directions  
434 (Figure S3) with no clear relationship between the strike angles and faulting types.

435 Additional insights on dominant loading mechanisms and crustal stress  
436 parameters in different areas can be obtained by comparing the stress inversion results  
437 with surface strain-rate from geodetic data in regions with/out topography and with/out  
438 inferred deep creep (e.g. Townend and Zoback, 2006). Deriving focal mechanisms for  
439 smaller events will allow stress inversions to be done using smaller sub-volumes and time  
440 intervals, leading to better resolution of stress variations in space and time. Numerical  
441 simulations of stress/strain evolution in crustal models with different loadings, different  
442 fault geometries, and different in viscoelastic structures can aid the interpretation of  
443 results. These studies will be attempted in future work.

444

## 445 **6. Acknowledgments**

446 The earthquake and focal mechanism catalogs used in the paper are available in  
447 the Southern California Earthquake Data Center (<https://scedc.caltech.edu/>). The study  
448 was supported by the Southern California Earthquake Center (based on NSF Cooperative  
449 Agreement EAR-1600087 and USGS Cooperative Agreement G17AC00047) and the  
450 U.S. Department of Energy (award DE-SC0016520).. PMG acknowledges funding from  
451 the Helmholtz Association in the frame of the Young Investigators Group VH-NG-1232  
452 (SAIDAN).

453

## 454 **7. References**

455 Aben, F. M., Brantut, N., Mitchell, T. M., & David, E. C. (2019). Rupture  
456 energetics in crustal rock from laboratory-scale seismic tomography. *Geophysical*  
457 *Research Letters*, *46*(13), 7337-7344.

458 Abolfathian, N., Martínez-Garzón, P., & Ben-Zion, Y. (2019). Spatiotemporal  
459 variations of stress and strain parameters in the San Jacinto fault zone. *Pure and Applied*  
460 *Geophysics*, *176*(3), 1145-1168.

461 Ben-Zion, Y., & Sammis, C. G. (2003). Characterization of fault zones. *Pure and*  
462 *Applied Geophysics*, *160*(3-4), 677-715.

463 Ben-Zion, Y., & Zaliapin, I. (2019). Spatial variations of rock damage production  
464 by earthquakes in southern California. *Earth and Planetary Science Letters*, *512*, 184-  
465 193.

466 Bott, M. H. P. (1959). The mechanics of oblique slip faulting. *Geological*  
467 *Magazine*, *96*(02), 109-117.

468 Cooke, M. L., & Beyer, J. L. (2018). Off-Fault Focal Mechanisms Not  
469 Representative of Interseismic Fault Loading Suggest Deep Creep on the Northern San  
470 Jacinto Fault. *Geophysical Research Letters*, *45*(17), 8976-8984.

471 Fialko, Y., Rivera, L., & Kanamori, H. (2005). Estimate of differential stress in  
472 the upper crust from variations in topography and strike along the San Andreas fault.  
473 *Geophysical Journal International*, *160*(2), 527–532.

474 Fuis, G. S., Scheirer, D. S., Langenheim, V. E., & Kohler, M. D. (2012). A new  
475 perspective on the geometry of the San Andreas fault in southern California and its  
476 relationship to lithospheric structure. *Bulletin of the Seismological Society of*  
477 *America*, *102*(1), 236-251.

478 Hardebeck, J. L. (2014). The impact of static stress change, dynamic stress  
479 change, and the background stress on aftershock focal mechanisms. *Journal of*  
480 *Geophysical Research: Solid Earth*, *119*(11), 8239-8266.

481 Hardebeck, J. L., & Hauksson, E. (2001). Crustal stress field in southern  
482 California and its implications for fault mechanics. *Journal of Geophysical Research:*  
483 *Solid Earth*, *106*(B10), 21859-21882.

484 Hardebeck, J. L., & Michael, A. J. (2006). Damped regional-scale stress  
485 inversions: Methodology and examples for southern California and the Coalinga  
486 aftershock sequence. *Journal of Geophysical Research: Solid Earth*, *111*(B11).

487 Hartigan, J. A., & Wong, M. A. (1979). Algorithm AS 136: A k-means clustering  
488 algorithm. *Journal of the Royal Statistical Society. Series C (Applied Statistics)*, *28*(1),  
489 100-108.

490 Hauksson, E., Yang, W., & Shearer, P. M. (2012). Waveform relocated  
491 earthquake catalog for southern California (1981 to June 2011). *Bulletin of the*  
492 *Seismological Society of America*, *102*(5), 2239-2244.

493 Lockner, D. A., Byerlee, J. D., Kuksenko, V., Ponomarev, A., & Sidorin, A.  
494 (1992). Observations of quasistatic fault growth from acoustic emissions. In *International*  
495 *Geophysics* (Vol. 51, pp. 3-31). Academic Press.

496 Lund, B., & Townend, J. (2007). Calculating horizontal stress orientations with  
497 full or partial knowledge of the tectonic stress tensor. *Geophysical Journal*  
498 *International*, 170(3), 1328-1335.

499 Lyakhovsky, V., & Ben-Zion, Y. (2009). Evolving geometrical and material  
500 properties of fault zones in a damage rheology model. *Geochemistry, Geophysics,*  
501 *Geosystems*, 10(11), Q11011.

502 Lyakhovsky, V., Ben-Zion, Y., & Agnon, A. (1997). Distributed damage,  
503 faulting, and friction. *Journal of Geophysical Research: Solid Earth*, 102(B12), 27635-  
504 27649.

505 Martínez-Garzón, P., Ben-Zion, Y., Abolfathian, N., Kwiatak, G., & Bohnhoff,  
506 M. (2016a). A refined methodology for stress inversions of earthquake focal  
507 mechanisms. *J. Geophys. Res.*, 121, 8666-8687.

508 Martínez-Garzón, P., Kwiatak, G., Bohnhoff, M., & Dresen, G. (2016b). Impact  
509 of fluid injection on fracture reactivation at The Geysers geothermal field. *Journal of*  
510 *Geophysical Research: Solid Earth*, 121(10), 7432-7449.

511 Martínez-Garzón, P., Kwiatak, G., Ickrath, M., & Bohnhoff, M. (2014). MSATSI:  
512 A MATLAB package for stress inversion combining solid classic methodology, a new  
513 simplified user-handling, and a visualization tool. *Seismological Research Letters*, 85(4),  
514 896-904.

515 Matti, J. C., Morton, D. M., & Powell, R. E. (1993). Paleogeographic evolution of  
516 the San Andreas fault in southern California: A reconstruction based on a new cross-fault  
517 correlation. *The San Andreas fault system: Displacement, palinspastic reconstruction,*  
518 *and geologic evolution*, 178, 107-159.

519 McCloskey, J., Nalbant, S. S., Steacy, S., Nostro, C., Scotti, O., & Baumont, D.  
520 (2003). Structural constraints on the spatial distribution of aftershocks. *Geophysical*  
521 *research letters*, 30(12).

522 McKenzie, D. P. (1969). The relation between fault plane solutions for  
523 earthquakes and the directions of the principal stresses. *Bulletin of the Seismological*  
524 *Society of America*, 59(2), 591-601.

525 Michael, A. J. (1984). Determination of stress from slip data: faults and  
526 folds. *Journal of Geophysical Research: Solid Earth*, 89(B13), 11517-11526.

527 Michael, A. J. (1987). Use of focal mechanisms to determine stress: a control  
528 study. *Journal of Geophysical Research: Solid Earth*, 92(B1), 357-368.

529 Ozakin, Y., & Ben-Zion, Y. (2015). Systematic receiver function analysis of the  
530 Moho geometry in the Southern California Plate-Boundary region. *Pure and Applied*  
531 *Geophysics*, 172(5), 1167-1184.

532 Spotila, J. A., Farley, K. A., Yule, J. D., & Reiners, P. W. (2001). Near-field  
533 transpressive deformation along the San Andreas fault zone in southern California, based  
534 on exhumation constrained by (U-Th)/He dating. *Journal of Geophysical Research:*  
535 *Solid Earth*, 106(B12), 30909-30922.

536 Townend, J., & Zoback, M. D. (2006). Stress, strain, and mountain building in  
537 central Japan. *Journal of Geophysical Research: Solid Earth*, 111(B3).

538 Vavryčuk, V. (2011). Principal earthquakes: Theory and observations from the  
539 2008 West Bohemia swarm. *Earth and Planetary Science Letters*, 305(3-4), 290-296.

540 Vavryčuk, V. (2014). Iterative joint inversion for stress and fault orientations  
541 from focal mechanisms. *Geophysical Journal International*, 199(1), 69-77.

542 Wallace, R. E. (1951). Geometry of shearing stress and relation to faulting. *The*  
543 *journal of Geology*, 59(2), 118-130.

544 Wdowinski, S. (2009). Deep creep as a cause for the excess seismicity along the  
545 San Jacinto fault. *Nature Geoscience*, 2(12), 882-885.

546 Yang, W., & Hauksson, E. (2013). The tectonic crustal stress field and style of  
547 faulting along the Pacific North America Plate boundary in Southern  
548 California. *Geophysical Journal International*, 194(1), 100-117.

549 Yang, W., Hauksson, E., & Shearer, P. M. (2012). Computing a large refined  
550 catalog of focal mechanisms for southern California (1981-2010): Temporal stability of  
551 the style of faulting. *Bulletin of the Seismological Society of America*, 102(3), 1179-1194.

552 Yule, D., & Sieh, K. (2003). Complexities of the San Andreas fault near San  
553 Gorgonio Pass: Implications for large earthquakes. *Journal of Geophysical Research:*  
554 *Solid Earth*, 108(B11).

555 Zaliapin, I., & Ben-Zion, Y. (2013). Earthquake clusters in southern California I:  
556 Identification and stability. *Journal of Geophysical Research: Solid Earth*, 118(6), 2847-  
557 2864.

558 Zaliapin, I., & Ben-Zion, Y. (2020). Earthquake declustering using the nearest-  
559 neighbor approach in space-time-magnitude domain, *Journal of Geophysical Research*,  
560 doi: 10.1029/2018JB017120.

561 Zoback, M. L. (1992). First- and second-order patterns of stress in the lithosphere:  
562 The World Stress Map Project. *Journal of Geophysical Research: Solid Earth*, 97(B8),  
563 11703-11728.

564 Zhu, L., & Kanamori, H. (2000). Moho depth variation in southern California  
565 from teleseismic receiver functions. *Journal of Geophysical Research: Solid*  
566 *Earth*, 105(B2), 2969-2980.

**Table 1.** Seismic statistics in SCTR, comparing foreshocks, mainshocks, and aftershocks.

<b>1981 to 2017 -1 to 30 km depth</b>	<b>No. of events</b>	<b>No. of events %</b>	<b>Seismogenic thickness (90%)</b>	<b>Maximum Magnitude (90%)</b>	<b>Mean Magnitude</b>	<b>Median Magnitude</b>
<b>Foreshock</b>	2,128	14.2	16.8	2.63	2.28	2.21
<b>Mainshock</b>	3,218	21.5	16.9	3.12	2.51	2.37
<b>AfterShock</b>	9,648	64.3	13.5	2.94	2.42	2.3

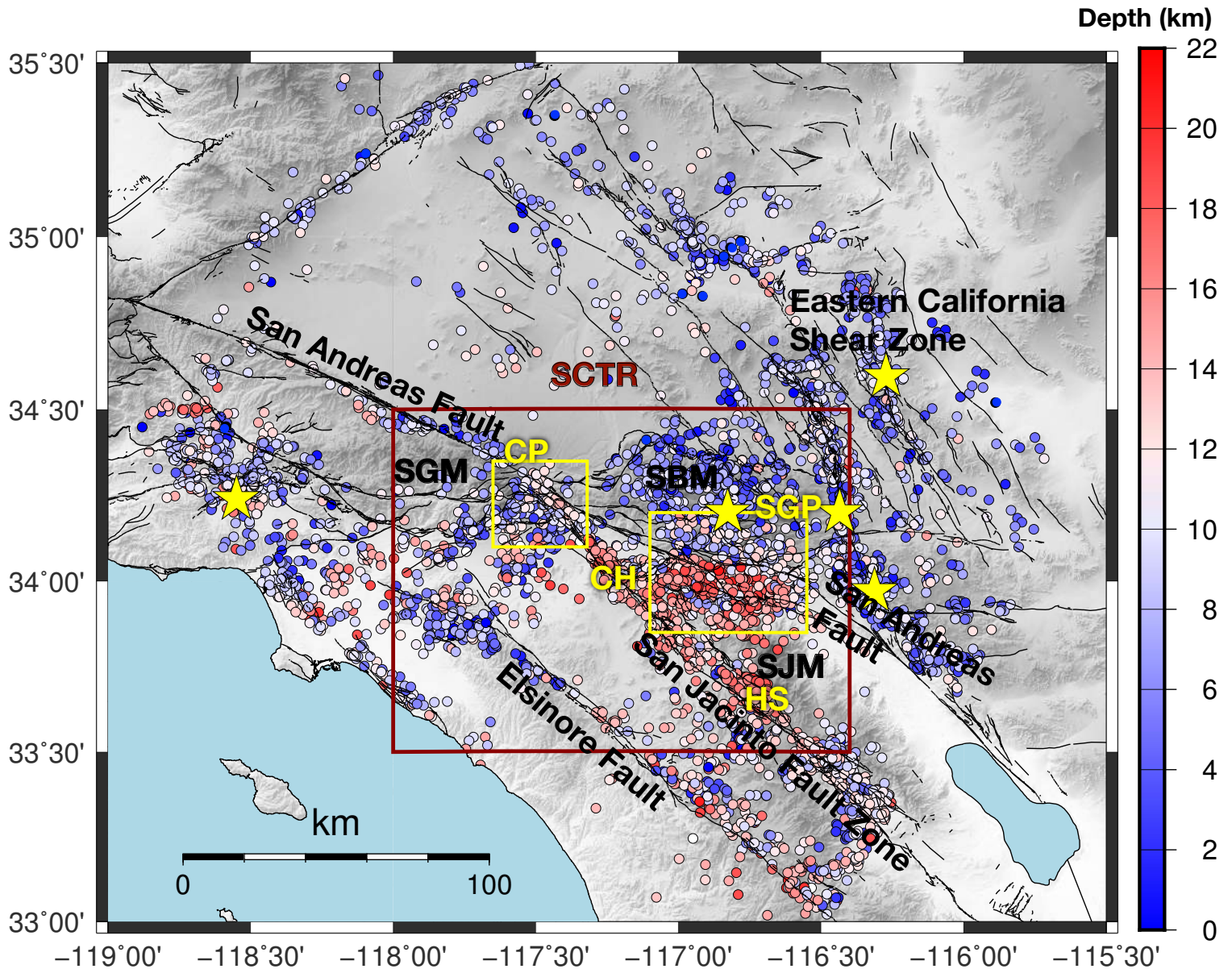


**Figure 1.** Distribution of declustered seismicity with focal mechanisms in the selected region in Southern California, between 1981 to 2017 used for the stress inversion. Each event is color-coded with its hypocentral depth. The brown rectangle denotes a selected region around the South Central Transverse Ranges (SCTR). The yellow squares show focused regions of study, Cajon Pass (CP), and San Gorgonio Pass (SGP). Faults are marked in black lines. Stars show events larger than magnitude 6 in the region during the selected time period. SCTR and yellow fonts in the figure shows regions of study, while black fonts defines geology of the area. (SGM: San Gabriel Mountains; SBM: San Bernardino Mountains; SJM: San Jacinto Mountains; CH: Crafton Hills; HS: Hot Springs).

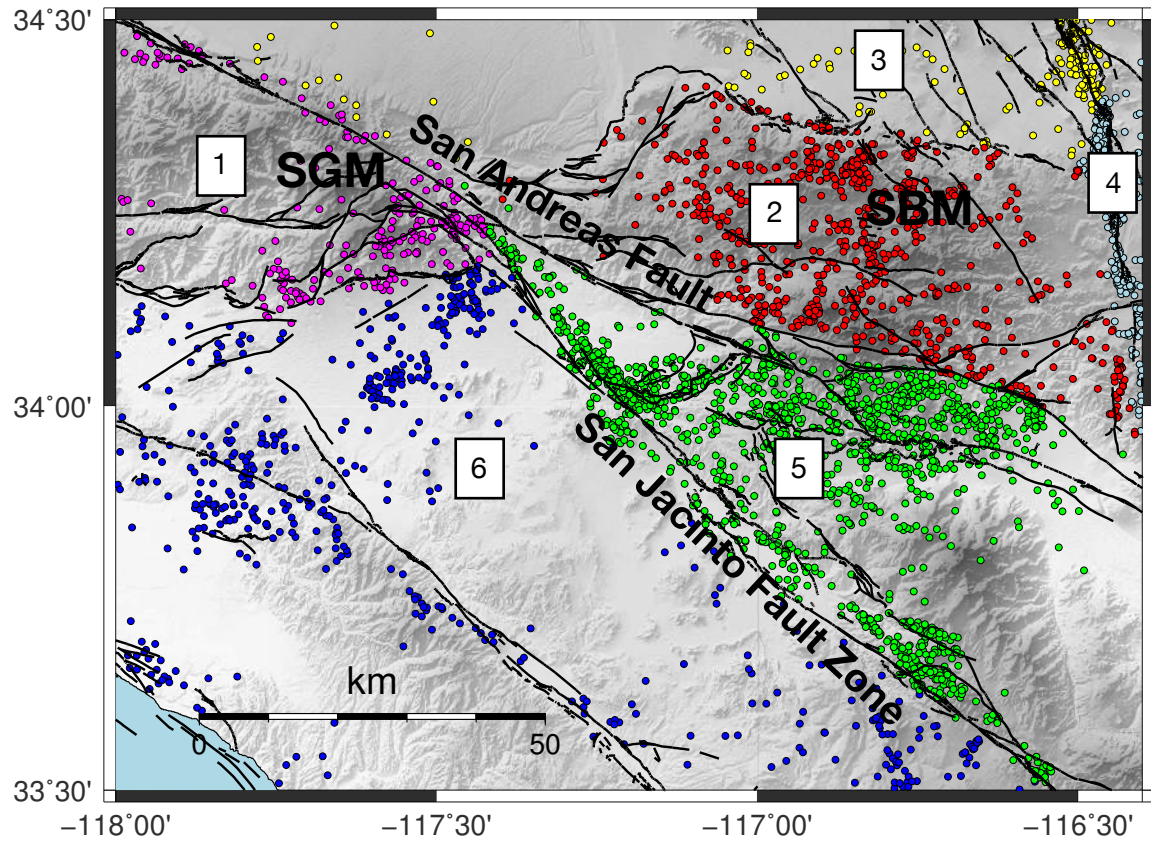


**Figure 2.** Seismicity distribution in six subregions in the selected region around the South Central Transverse Ranges: (1) San Gabriel Mountains (SGM) in purple, (2) San Bernardino Mountains (SBM) in red, (3) northern part in yellow, (4) eastern section of the SBM in cyan, (5) between the San Andreas Fault (SAF) and San Jacinto Fault Zone (SJFZ) in green, (6) western section of the SJFZ in blue.

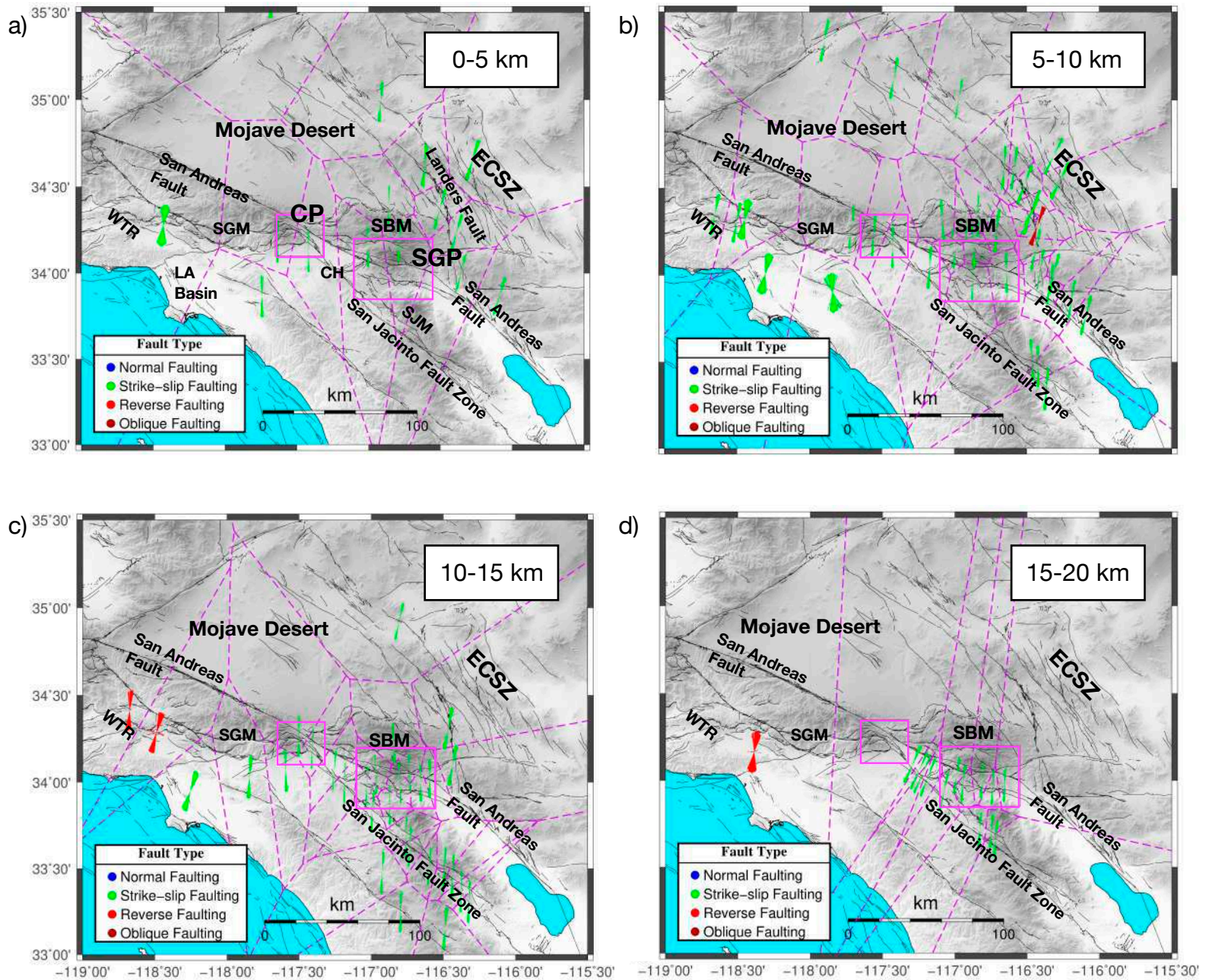


**Figure 3.** Regional distribution of the maximum horizontal compressional stress orientations ( $S_{Hmax}$ ) at (a) 0 to 5 km, (b) 5 to 10 km, (c) 10 to 15 km, (d) 15 to 20 km depth sections. The variations in  $S_{Hmax}$  orientations show the uncertainty of 95% confidence interval. The orientations are color-coded in red, green, blue, and brown denoting reverse, strike-slip, normal and oblique faulting, respectively. Purple dashed lines indicate the used Voronoi cells. WTR: West Transverse Ranges; SGM: San Gabriel Mountains; CP: Cajon Pass; CH: Crafton Hills; SJM: San Jacinto Mountains; SGP: San Gorgonio Pass; SBM: San Bernardino Mountains; ECSZ: Eastern California Shear Zone.

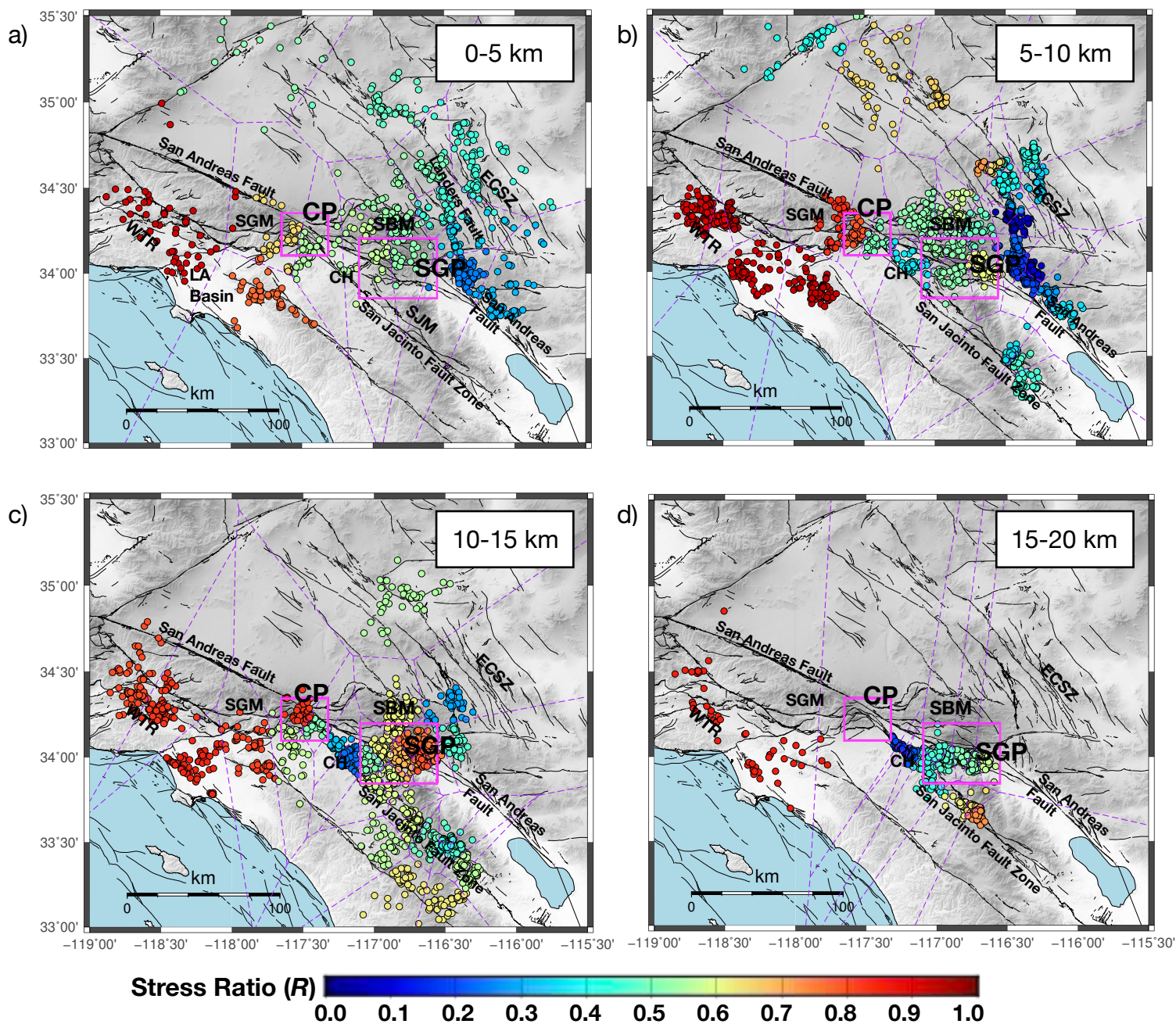


**Figure 4.** Regional seismicity distribution color-coded with values of the stress ratio  $R$  at (a) 0 to 5 km, (b) 5 to 10 km, (c) 10 to 15 km, (d) 15 to 20 km depth sections. In a strike-slip faulting environment,  $R$ -values around 0.5, 0 and 1 indicate pure strike-slip, transtensional and transpressional stress regimes, respectively. Purple dashed lines indicate the used Voronoi cells.

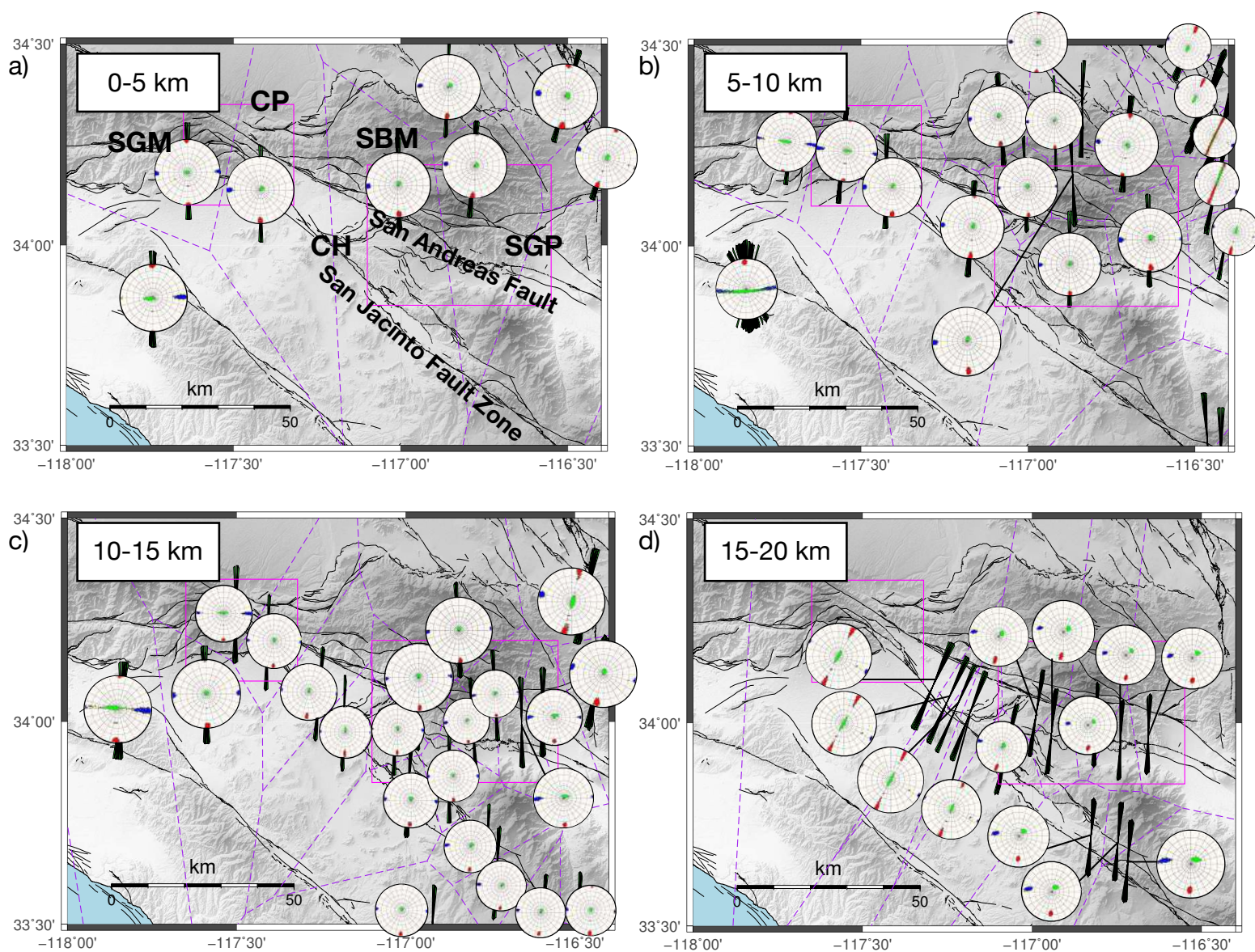


**Figure 5.** Distribution of the maximum horizontal compressional stress orientations ( $S_{Hmax}$ ) in fan symbols and the principal stress orientations (Stereonet) in the selected region around SCTR at (a) 0 to 5 km, (b) 5 to 10 km, (c) 10 to 15 km, (d) 15 to 20 km depth sections. The variations in  $S_{Hmax}$  orientations show the uncertainty of 95% confidence interval. The maximum, intermediate and minimum principal stresses in the stereonet are indicated with red, green, and blue, respectively. Purple dashed lines indicate the used Voronoi cells. CP and SGP shown in pink rectangles.

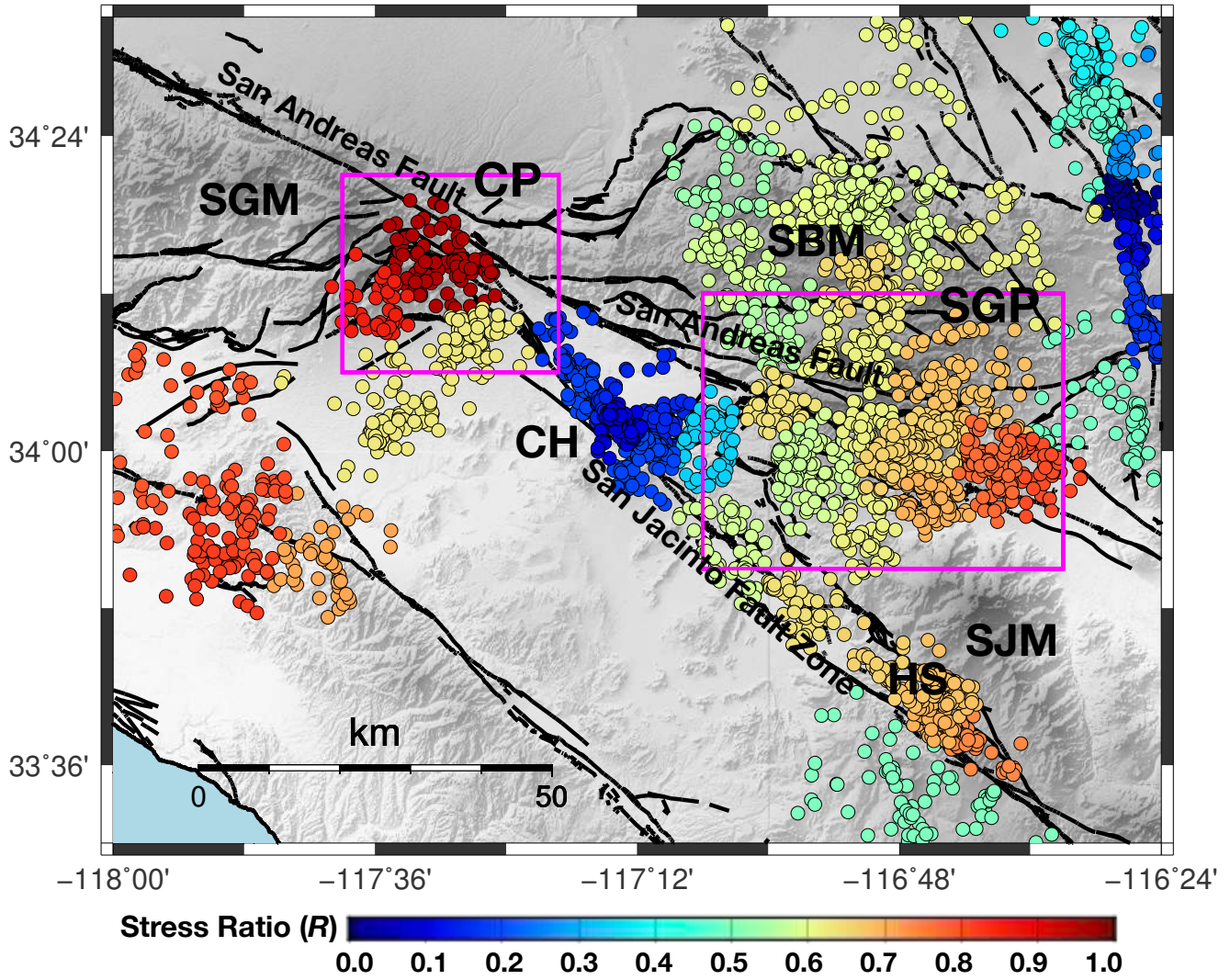


**Figure 6.** Seismicity color-coded with values of the stress ratio  $R$  in the selected region around SCTR. Background seismicity distributed in 6 sections based on figure 2. Signs are as in figures 4.



**Figure 7.** Seismicity color-coded with values of the stress ratio  $R$ , at (a,b) 0 to 5 km, (c,d) 5 to 10 km, (e,f) 10 to 15 km, (g,h) 15 to 20 km depth sections. Subplots (a,c,e,g) show the variation of the stress ratio regarding to the mainshocks while (b,d,f,h) are estimated inverting the aftershock events. Signs are as in figures 4.

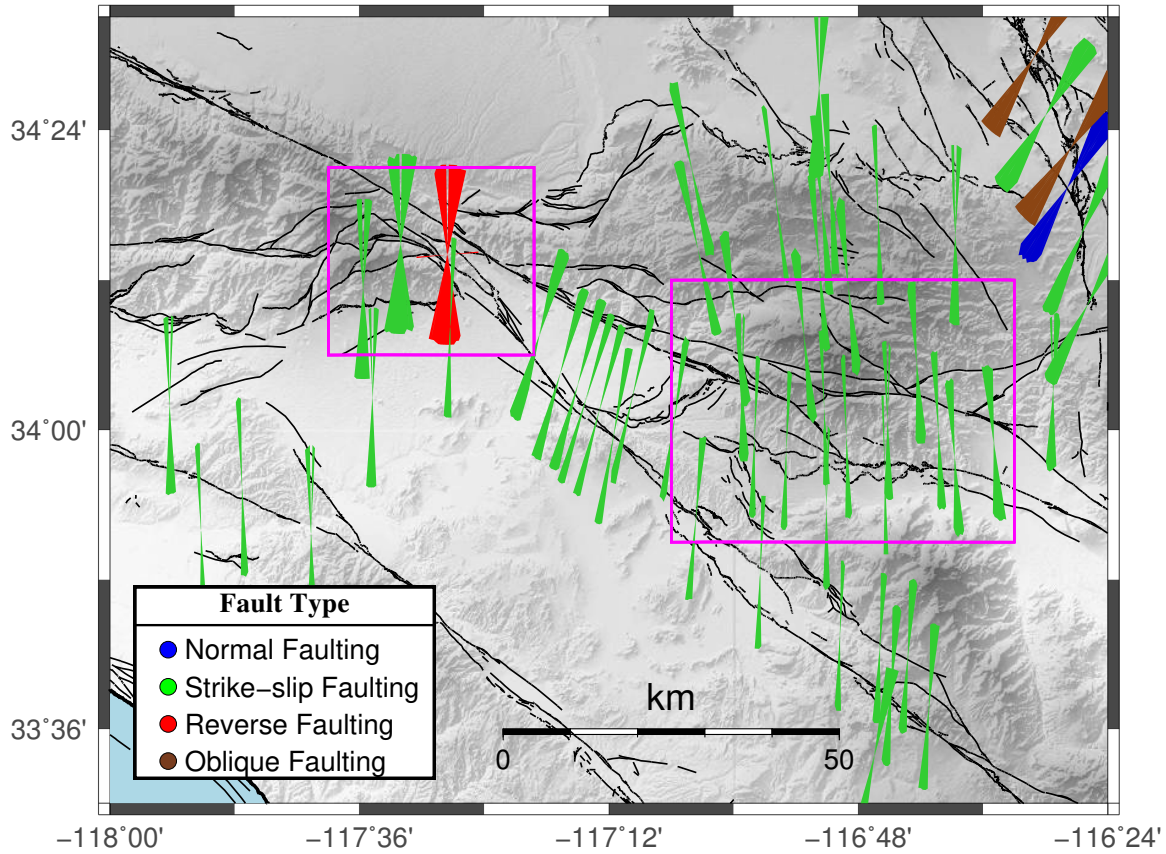


**Figure S1.** Distribution of the maximum horizontal compressional stress orientations ( $S_{Hmax}$ ) in the selected region around SCTR based on data distribution in six subregions as in Figure 2. Signs are as in Figure 3.

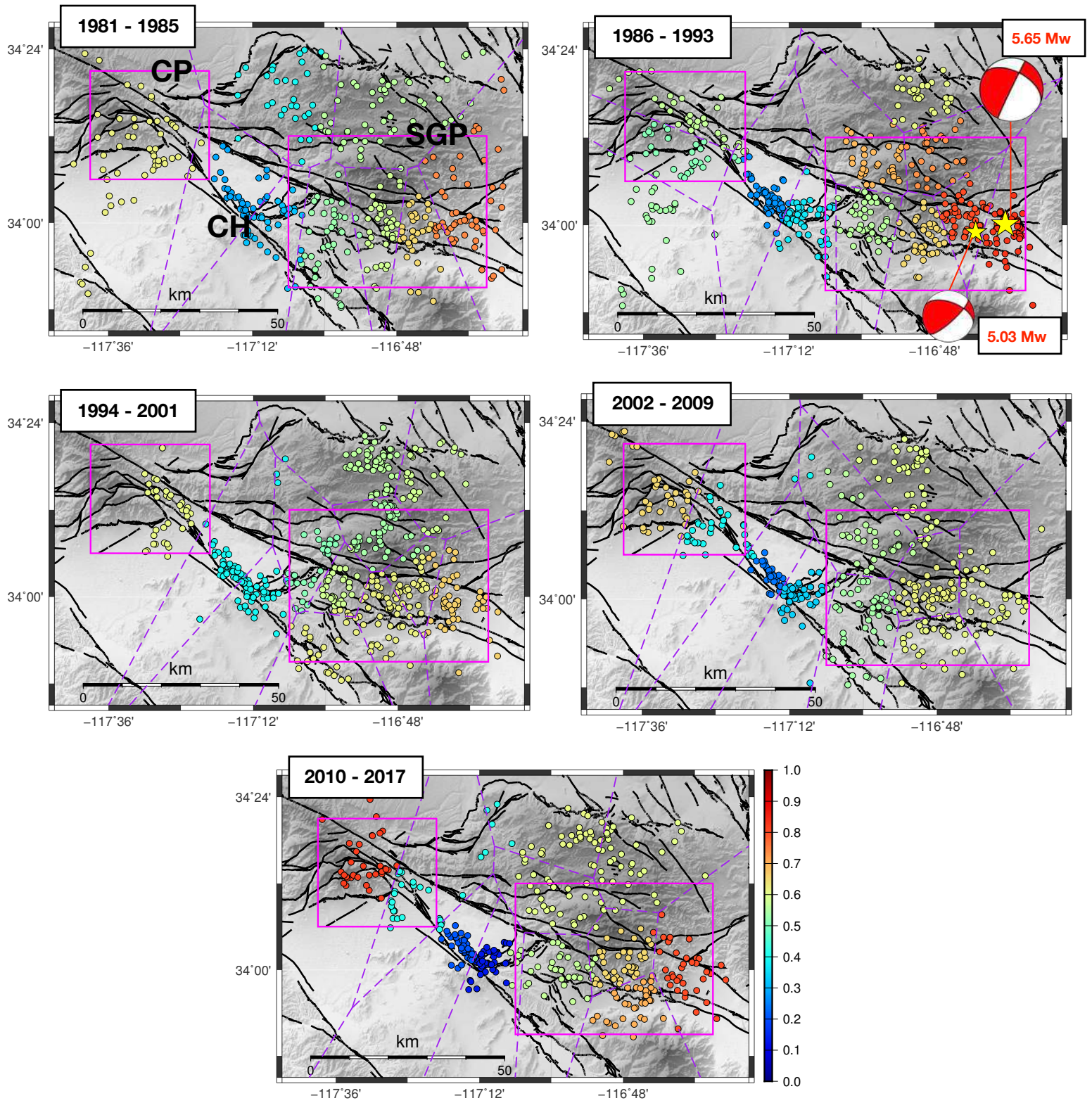


**Figure S2.** Temporal Variations of stress ratios near CP and SGP. Signs are as in Figure 4.

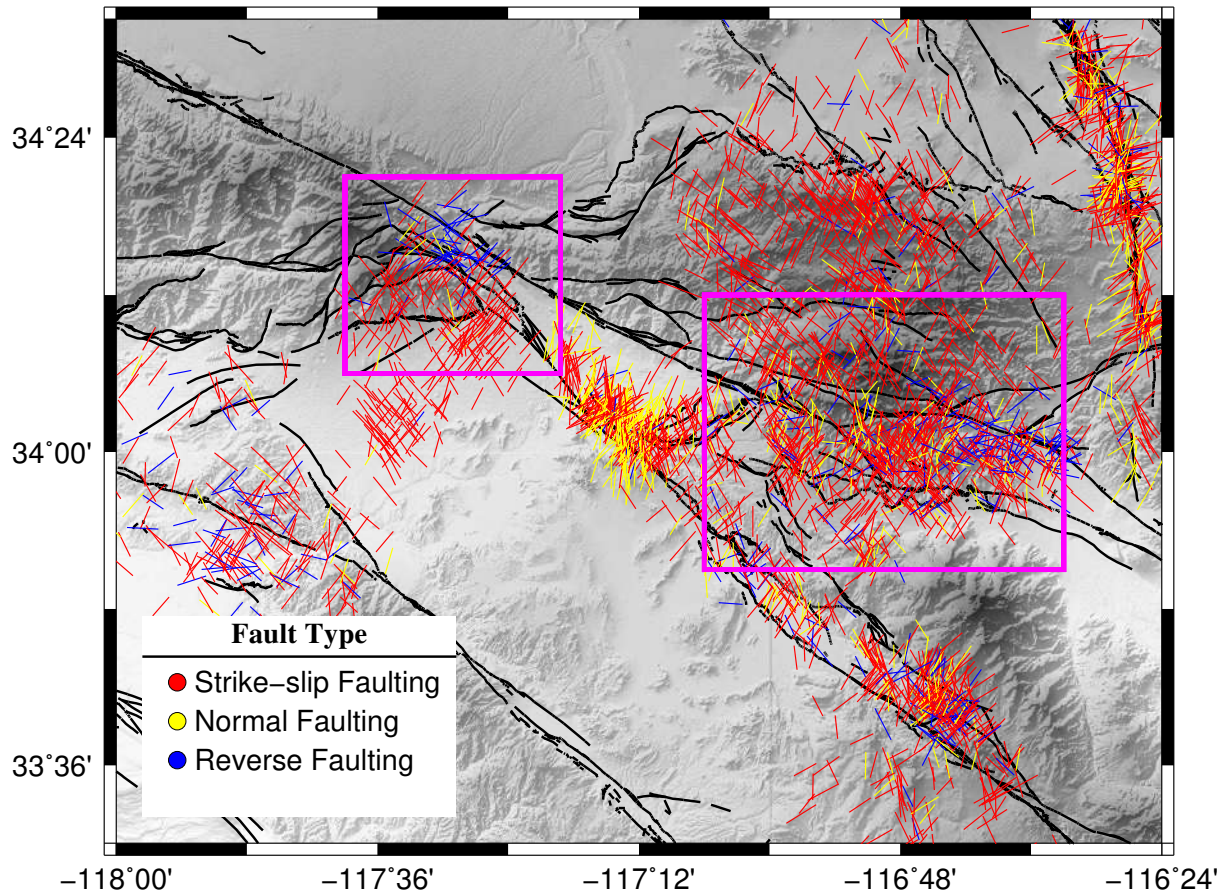


**Figure S3.** Distribution of the strike angles of the focal mechanisms from the declustered catalog, color-coded with the main types of faulting in the selected region around SCTR based on data distribution in six subregions as in Figure 2.